A Novel Principle to Localize Scattered-wave Sensitivity Using Wave Interference and Its Adjoint

Shohei Minato (s.minato-1@tudelft.nl)
Delft University of Technology
Ranajit Ghose
Delft University of Technology

Research Article

Keywords: spatiotemporal distribution, heterogeneities, interferences observed, disciplines and scales

Posted Date: March 30th, 2021

DOI: https://doi.org/10.21203/rs.3.rs-358569/v1

A novel principle to localize scattered-wave sensitivity using wave interference and its adjoint

Shohei Minato[1]*, Ranajit Ghose[1]

[1]Dept. of Geoscience and Engineering, Delft University of Technology, Stevinweg 1, 2628 CN Delft, Netherlands.

*Correspondence to: s.minato-1@tudelft.nl

Abstract

When using scattered waves for high-resolution imaging of a medium, the sensitivity of these waves to the spatiotemporal distribution of heterogeneities is undoubtedly a key factor. The traditional principle behind using scattered waves to detect small changes suffers from an inherent limitation when other structures, not of interest, are present along the wave propagation path. We propose a novel principle that leads to enhanced localization of wave sensitivity, without having to know the intermediate structures. This new principle emerges from a boundary integral representation which utilizes wave interferences observed at multiple points. When tested on geophysical acoustic wave data, this new principle leads to much better sensitivity localization and detection of small changes in seismic velocities, which were otherwise impossible. Overcoming the insensitivity to a target area, it offers new possibilities for imaging and monitoring small changes in properties, which is critical in a wide range of disciplines and scales.

Introduction

Scattered waves and their sensitivity to heterogeneity are fundamentally important to study any kind of material structure. The sensitivity represents how much changes in wave scattering is associated with changes in the heterogeneity. A knowledge of the sensitivity and its distribution enables one to address why, how and where such changes occur[1–4].

When the heterogeneities are known, then one can model the scattered wave data. The sensitivity (Jacobian) derived from the modelled data can be used to predict how those heterogeneities in natural or engineered composite materials interact when subjected to external stimuli[1–3]. When the heterogeneities are not known, the sensitivity is derived from the observed data. In this case, the sensitivity is defined as a change (gradient) in the difference between the observed waveform and the waveform estimated based on a physical principle, as a result of changes in the assumed model[4–6]. In this article, we address this latter sensitivity issue. This is important in many real-world problems that involve resolving and monitoring unknown heterogeneities. For example, the sensitivity derived from acoustic, electromagnetic, or seismic scattered waves is key to *in-vivo* medical imaging to identify tumors[7,8], *in-situ* seismological monitoring of geological materials (e.g., rock, soil, ice, fluid)[6,9,10], and health monitoring of civil engineering structures (e.g., metal and concrete)[11].

The conventional principle behind calculating wave sensitivity involves one source point, one observation point, and the Huygens' principle[4–6]: an incident wave at a source point causes a disturbance in the material, a secondary wavefield is generated at a heterogeneity, and the total wavefield (incident and scattered waves) is measured at an observation point. The sensitivity is then calculated using two Helmholtz equations: one in which the incident wave propagates forward in time from the source point, and one in which scattered waves propagate backward in time from the observation point (adjoint). These two wavefields have identical arrival times at the location where scattered waves are generated

(i.e., at the location of the heterogeneity). The sensitivity of the scattered waves is calculated by analyzing the amount of correlation between the two wavefields[4–6].

In various disciplines, owing to the reduced footprint of sensors and the increased computational resources, measurements and data processing based on many spatial observation points have become common. For example, scattered waves are measured with spatially dense sampling, e.g., on the surface of the Earth[12,13] or along boreholes[14,15], at the surface of or inside the human body[16,17], and in civil engineering structures[16,18]. These developments have led to spatially and temporally high-resolution imaging of materials across scales[12,15,19–21].

Using the conventional principle, the sensitivity from multiple sets of source-observation points is obtained by simply summing up the sensitivity from every single set[4–6], due to the linearity of the problem. Although this approach improves the sensitivity estimation, it does not fully exploit the interrelation among the scattered waves. As the conventional physical principle addresses material heterogeneity present along the wave propagation paths starting from a source and ending at an observation point, small material perturbation between the observation points does not matter, unless the heterogeneities around the source points and those present along the source-observation paths are sufficiently known. This limits resolving the temporal changes in many applications. For example, in geophysical monitoring, wave sources at the Earth's surface and buried receivers are often deployed to monitor stress and/or fluid in the underground[22–24]. In addition to time-lapse changes in the target area, such monitoring data, however, also contain the effect of time-lapse changes around a source point, e.g., due to environmental effects (like rainfall), which can jeopardize entire time-lapse monitoring efforts[23].

In this article, we present a novel physical principle for calculating and localizing the sensitivity without having to know the heterogeneities around the source points and those

along the path from the source to the observation point. As in the conventional approach, the new principle is based on the correlation between forward and backward propagating waves. However, utilizing a boundary integral representation, here the observed waves and their interferences are exploited in correlating the wavefields, in order to take into account the information shared by multiple observation points (including all wave phenomena occurring along the path, e.g., transmission, scattering and dissipation). This leads to capturing small changes in the material properties, which remain otherwise hidden.

In the following discourse, we discuss the new physical principle and show the key concept behind calculating the wave sensitivity in a data-driven manner using multiple observation points and the boundary integral representation. In order to do this, we first present the evidence that this representation works in real-world data of scattered waves observed in the field, and illustrate how the novel principle localizes the sensitivity. Successful localization of sensitivity and resolution of material heterogeneities are then verified on an experimental dataset. Next, we explore the potential use of this localized sensitivity to quantify temporal variations of acoustic properties in saturated rocks due to changes in pore-pressure associated with subsurface fluid flow. Finally, we discuss the possibilities for various observation geometries and applications.

Results

The boundary integral representation

When scattered waves are observed at multiple locations, a part of the wavefield containing information of the wave phenomena (transmission, scattering and dissipation) is common to different observation points. Such information, which relates a response at one place to that at other places, has extensively been explored in classical wave theory by means

of the boundary integral representation of wavefields[25]. We adapt this representation in order to localize the sensitivity.

As shown in Fig. 1a, suppose that scattered waves are observed at multiple locations consisting of a single observation point P and an array of observation points marked as "reference receiver array". Assuming a two-dimensional, scalar Helmholtz equation, we can adapt a boundary integral representation to calculate the response at P by extrapolating waves recorded at the reference receiver array (see "Methods"). The vertical array for the reference receivers, as shown in. Fig. 1a, is same as what we have used in the field experiment. However, this array can be arbitrary in shape. Let us consider an acoustic wavefield where the fluid pressure in a fluid-filled borehole due to a pressure source at the surface is measured. The measured data are preprocessed such that they represent a 2D wave propagation (see Supplementary Note 1). Note that these 2D measurements correspond to, e.g., surface-wave measurements using seismometer arrays[12], electromagnetic wave experiments using boreholes[26], non-destructive material testing using embedded sensors[18], or ultrasonic/microwave medical imaging with an array of surface/embedded sensors at/in the human body[17,27,28].

At first the modelled impulse responses ("model-driven waves" in Fig. 1a), representing responses at the reference receiver array for an impulse at P, are calculated assuming a model which is independent of the structure around the source point at S (gray-shaded area in Fig. 1a). This is because the model-driven waves do not radiate outward from the considered Dirichlet boundary (also commonly known as sound-soft or free-surface boundary) at the location of the reference receiver array. Then the boundary integral representation performs a temporal convolution between the model-driven waves and the observed waveforms at the reference receiver array ("data-driven waves" in Fig. 1a). This corresponds to the summation of traveltimes for travelpaths from S to the reference receiver

array and that from P to the same array. The final response at P ("extrapolated waveform") is then obtained by collecting and adding contributions coming from all receivers in the reference array (Fig. 1b).

A part of the receivers (the area enclosed by the green dotted lines in Figs. 1a,b) in the reference array dominantly contributes to the final response due to the stationary phase, considering the Fresnel volume[29]. This indicates that all wave phenomena (transmission, scattering, and dissipation), which take place earlier than the time of arrival of the wave at the reference receiver array from the source S, are accounted for in a data-driven manner without a model. When we assume a realistic velocity model to calculate the model-driven waves, the extrapolated waveform matches excellently with the directly observed waveform (Fig. 1c). In the field data example shown in Fig. 1, the velocity model is derived from measurements of acoustic velocity at two vertical boreholes.

The result in Fig. 1c clearly shows that the boundary integral representation works very well on the real-world scattered wave data, and that it is possible to extrapolate responses at the observation point P without knowing the model around the source point S.

A novel principle

Assuming negligible extrapolation error, any difference between the extrapolated and the directly observed waveforms is an indication that the assumed model deviates from the true model. Therefore, the sensitivity is defined as a change in the difference between the extrapolated and the observed waveforms due to a change in the assumed model[4–6].

Let us consider a material which contains multiple scatterers (black circles in Fig. 2a). The measurement geometry is similar to Fig. 1a. Suppose that a local scatterer Q has a smaller scattering strength than the other scatterers. A waveform at the observation point P is extrapolated using the boundary integral representation and assuming homogeneity around P

(the medium to the left of the vertical receiver array in Fig. 2a is assumed homogeneous, while the gray-shaded part on the right located close to the source does not need any such assumption). Since the boundary integral representation is independent of the knowledge of any heterogeneity around the source, any difference between the observed and the extrapolated waveforms is caused by a disturbance in the wavefield due to the local scatterer Q located close to the observation point P (red arrows in Fig. 2a), and does not have any effect of the scattering (black arrows in Fig. 2a) that occurs around the source point. This feature improves the sensitivity to the local scatterer Q, without the need to know the position and/or the nature of the scatterers located between the source point and the reference receiver array (gray-shaded area in Fig. 2a).

Using the difference waveform, we now introduce a novel physical principle based on the boundary integral representation. Application of the adjoint-state method[4,30] to the discretized equations (see "Methods") enables us to explain the principle using two wave-propagation thought experiments: forward and backward propagations, as shown in Fig. 2b. In the forward propagation experiment, suppose that an impulsive wave propagates from the observation point P to a hypothetical scatterer Q'. The green arrow in Fig. 2b shows the wave propagating forward in time with traveltime larger than zero. Next, in the backward propagation experiment, the difference waveform (red arrows in Fig. 2a) is crosscorrelated with the data-driven waves (observed waveforms at the reference receiver array) and then back-propagated in time from the reference receiver array to the hypothetical scatterer Q'. This gives the model-driven and data-driven waves shown by the blues arrows in Fig. 2b. These arrows illustrate the above-described process, marking backward propagation in time for waves with traveltimes smaller than zero.

Note that crosscorrelation corresponds to subtraction of traveltimes; therefore the data-driven waves are represented by the blue arrows in Fig. 2b. Consequently, collecting all

contributions from the reference receiver array and adding them result in the scattered waves (red arrows in Fig. 2b) which propagate backward from the hypothetical scatterer to the source point, leaving only the forward propagating wave travelling from Q to P (green arrow in Fig. 2b). In this way, by analyzing the amount of correlation between the forward and the backward propagating waves, a large sensitivity can be achieved at the true scatterer Q in a data-driven manner, without having to know the heterogeneity around the source point.

This novel principle calculates the sensitivity which is highly localized at the location of the scatterer Q, without any knowledge of the complete heterogeneity distribution (Fig. 2c). In contrast, the sensitivity obtained from the conventional principle, using the same source-observation points, does not allow detecting the local scatterer Q (Fig. 2d). The same conclusion can be drawn even when we use all available data in the calculation (see Supplementary Fig. 1). When we assume that all heterogeneities but Q are perfectly known, the conventional sensitivity approaches the localized sensitivity that we estimate using the new principle (Fig. 2e). In other words, the conventional principle can address small heterogeneities only when the heterogeneities close to the source point are sufficiently known. On the other hand, the new principle, by exploiting interference of the observed scattered waves and its adjoint, makes it possible to localize the sensitivity very accurately, as if we have a-priori the complete and accurate knowledge of all heterogeneities.

Field test on sensitivity localization

We have tested this new sensitivity localization principle on field experimental data. The measurement geometry is same as in Fig. 1a, but here we have multiple observation points P located along another vertical line (Fig. 3a): in total we observe wavefield using two vertical arrays (left array, LA, and right array, RA). In the field test, this corresponds to measurements in two vertical boreholes.

For the sake of clarity, here we need to distinguish between extrapolated and calculated waveforms. Extrapolated waveforms are obtained using the boundary integral representation that we have presented above and assuming homogeneity (constant acoustic velocity). The calculated waveform, on the other hand, are the ones obtained through numerical (finite-difference, FD) computation also assuming homogeneity, where the source wavelet is estimated by deconvolution of the recorded waveform[31] with a waveform that is calculated assuming the same homogeneity and an impulsive source at S. Therefore, the difference in waveforms between the observation (black lines in Fig. 3b) and the calculation or extrapolation (green and red lines in Fig. 3b) indicates the deviation from the homogeneity. The waveforms calculated using the conventional approach by FD method (green lines in Fig. 3b) assumes a globally homogeneous material. On the other hand, those using the boundary integral representation (red lines in Fig. 3b) assumes local homogeneity between LA and RA, and heterogeneities around the source point (gray-shaded area in Fig. 3a) are accounted for in a data-driven manner. As a result, their waveforms vary over the receiver location (red lines in Fig. 3b), which implies an improved sensitivity to the local heterogeneity.

The sensitivity localization is evident in Fig. 4a. The conventional sensitivity shows large values around the source point S. Further, the conventional sensitivity varies smoothly in the subsurface, which implies small correlation between the incident and the scattered waves (averaging out of the contribution of different local scatterers). This is due to the fact that in the conventional approach, the difference waveforms have a complex nature as they include more scatterers (see black and green lines Fig. 3b). In contrast, the localized sensitivity, derived from the new principle found in this research, reveals a very detailed structure between LA and RA (Fig. 4a). The sensitivity indicates the amount of velocity perturbation/changes with respect to homogeneity, assuming Born scattering[32]. A comparison

with the heterogeneity directly observed at LA (Fig. 4b) shows that the localized sensitivity detects a much finer variation in heterogeneity than the conventional sensitivity at depths greater than 80 m. The novel principle exploits information in the observed data in a completely different manner than the conventional principle. As a result, the conventional sensitivity cannot achieve comparably good results even using all available data, including data from the reference receiver array (Supplementary Fig. 2).

Localized sensitivity: quantitative estimation of heterogeneity

The localized sensitivity can be exploited to resolve quantitatively the material heterogeneity. An inversion scheme can be formulated to estimate the acoustic velocity distribution by minimizing the difference between the observed and the calculated waveforms at the observation point. The localized sensitivity can navigate iteratively toward a best-fit model using nonlinear inversion (see "Methods") without a knowledge of the heterogeneity around the source points.

Using the same geometry as in Fig. 3a, multiple sources were used sequentially in the field to generate pressure waves at right to RA and left to LA (Fig. 5a) in order to illuminate the medium from various directions. The reference receiver array, the observation point (P), and the zone which does not contribute to calculating the localized sensitivity are appropriately defined depending on the source location (Fig. 5a). In order to verify a resolved heterogeneity, we additionally perform independent waveform measurements (ground-truthing) using downhole sources (Fig. 5b) and apply the conventional waveform inversion (Supplementary Note 2).

Waveform inversion estimates a velocity model starting from an initial guess[4–6]. We perform standard traveltime tomography to obtain the starting model (Fig. 6a). Waveforms around the first-arriving events and a frequency component similar to that in the independent

measurements using downhole sources are analyzed (Supplementary Notes 3 and 4). Figure 6b shows the estimated velocity structure using the localized sensitivity derived from the novel principle involving boundary integral representation. Figure 6c shows the result of waveform inversion where additional downhole sources have been placed in RA (ground-truthing). Figure 6d shows in details a comparison between the different velocity models. The estimated velocity using the localized sensitivity is strikingly close to the one obtained from independent waveform inversion using downhole sources and also to acoustic well log data at RA, especially at depths greater than 80 m where the raypath coverage is good (Fig. 6d).

Value of the enhanced localization of sensitivity in geophysical monitoring

The novel principle presented in this article localizes the sensitivity without any knowledge of the heterogeneity around a source point. This has a significant merit in overcoming the inherent limitations of time-lapse data analyses, where the accuracy of temporal changes occurring in a target area is important, but is affected by structures located outside the target area. Past seismic experiments have demonstrated that ignoring errors in source location[33] or near-surface changes due to seasonal variations in, e.g., water saturation[23] leads to spurious waveform changes and can jeopardize critical time-lapse seismic monitoring efforts. The use of the new principle enables overcoming these limitations by suppressing such spurious waveform changes (see Supplementary Notes 5).

We delve further into this concept through performing realistic synthetic monitoring tests. Although this novel principle can be useful in high-resolution monitoring in a wide variety of fields e.g., medical sciences, non-destructive material testing, civil engineering, in our synthetic test we consider geoscientific applications where monitoring is necessary while injecting fluid into the subsurface using boreholes. For example, recycled water is injected and stored in the aquifer for water resource management[34,35], or treated water is injected in

order to produce energy in geothermal fields or to store carbon dioxide in the subsurface[36]. In all these applications, detecting subsurface changes due to the replacement of fluid and changes in the pore pressure is crucial[34,37,38]. Monitoring using sensors located in the boreholes is generally performed for this purpose due to the sensitivity of downhole sensors to changes at the target depths[22–24] . Source points are located at the surface, as boreholes are generally inaccessible during the operation[35]. Therefore, we also consider the observation points located in boreholes and the source points at the surface (Fig. 7a), similar to field experiments discussed earlier in this article.

To generate realistic synthetic data, we assume a random velocity distribution with a mean velocity of 2.0 km/s (Fig. 7a). The data contain source location errors and errors due to temporal changes occurring outside the target area (the dashed rectangle in Fig. 7a). The target area is located at 100 m depth where the velocity decreases by 5 % with respect to the baseline measurement due to an increase in the pore pressure[39]. The topmost 6 meter is modeled as a vadose zone having a random velocity distribution with a mean value of 1.0 km/s (Supplementary Fig. 7). Additionally, the structure of the vadose zone is completely different between the baseline and the monitor surveys (Supplementary Fig. 7), representing a possible drastic change in seismic velocity in this zone due to seasonal change in water saturation[23,40]. Source-receiver geometry and frequency components are quite similar to those in the field experiments discussed earlier (Supplementary Note 6), except that the source location in the monitor survey contains random error up to 4 m (Supplementary Fig. 7).

We first look at the result of imaging the inter-borehole velocity heterogeneities in the baseline measurement. Here we consider two different scenarios for the prior information of the non-target zone (outside the two boreholes) to build an initial velocity model for waveform inversion. Assuming the same initial velocity model for depths greater than 16 m (Fig. 7b), we consider a situation where the correct average velocity and thickness of the

vadose zone are known (Fig. 7c), and in case we have a poor knowledge of them (Fig. 7d). These two different initial velocity models are used to estimate the heterogeneities using the conventional sensitivity (Figs. 7e,f) and the localized sensitivity (Figs. 7g,h), respectively. As the recorded waveforms contain information of the structure present along the wave propagation path connecting the surface source and the downhole receiver, the waveform inversion using the conventional sensitivity estimates the heterogeneities not only in between the boreholes but also outside, i.e., those structures to the left of LA and to the right of RA (Figs. 7e,f) - which are not of interest. More critically, the estimation of the velocity structure in between the borehole has been influenced by the accuracy in prior information of structures outside the two boreholes, contributing to large uncertainties in the estimated inter-borehole heterogeneities (Figs. 7i,j,k). On the contrary, the new principle presented in this research addresses the localized sensitivity and, therefore, provides directly the inter-borehole structure (Figs. 7g,h) which is minimally influenced by the accuracy in the prior information of the non-target zone (Fig. 7k).

In order to achieve accurate results using the conventional sensitivity, it is crucial to account for the propagation effects outside the target zone (gray-shaded area in Figs. 7g,h) by obtaining independently good prior information. Alternatively, one can design carefully a multi-scale inversion scheme utilizing sequentially data from lower to higher frequencies in order to avoid gaps in the wavenumber information[6]. However, this is not a trivial task due to the difficulty in acquiring low-frequency data using controlled sources[6] and because each frequency component has generally a different signal-to-noise ratio. The localized sensitivity is free from uncertainties associated with these fundamental limitations, because the propagation effects outside the target zone are accounted for in a data-driven manner.

Next we concentrate on the monitoring of time-lapse changes in the target zone which is located around 100 m depth (dashed rectangle in Fig. 7a). The results are shown in Fig. 8.

The new principle estimates the temporal changes at the target depth much better than the conventional approach (Figs. 8b,c). The conventional approach is sensitive to the source location errors in case an accurate prior information of the vadose zone is available (Supplementary Fig. 8). Generally, the conventional approach requires an accurate prior knowledge of the vadose zone (Fig. 7). Any inaccuracy in this prior knowledge results in a significant loss of accuracy in the estimated time-lapse changes at the target zone when using the conventional approach (Figs. 8c, 8e). On the contrary, the extremely high sensitivity of the new approach to the inter-well structures allows high-resolution estimation of the velocity changes, which is nearly independent of the presence of any source location error and/or inaccuracy in the prior information of the vadose zone (Figs. 8b, 8d, Supplementary Fig. 8).

Discussion

In this article, we present a novel principle to localize the sensitivity of scattered waves to medium heterogeneities, which otherwise remain hidden in case of using the conventional principle for sensitivity estimation. Earlier studies on Green's function retrieval[12,41–47], which is found useful in a variety of disciplines, e.g., medical diagnostics[44], seismology[12], exploration geophysics[42], and material testing[43], have tackled a similar problem from a different point of view. In those studies, the inter-receiver Green's function (impulse response) is estimated by effectively removing wave propagation paths from a source point using correlation or convolution[45]. Although there is a good similarity between Green's function retrieval and the concept presented here, there are also notable differences. First, in contrast with Green's function retrieval using crosscorrelation[45], our boundary integral representation can be applied to lossy media. This is a major difference. Furthermore, our primary purpose is to directly obtain the sensitivity using the adjoint of the boundary integral representation and, therefore, the associated Green's functions are by-products. This enables us to tackle the problem from a completely different point of view. We have used the

Dirichlet boundary condition in the Green's functions in a rather unconventional manner (see "Methods"). This makes it possible to relax the critical assumption of one-way wavefield propagation in the Green's function retrieval using convolution[46,47] and that of multi-component measurements or single-component measurements with approximations[45,48]. The assumption of one-way wavefield and/or the approximations due to the conventional boundary condition are otherwise necessary when the primary purpose is to retrieve Green's functions, which will require further processing.

We have formulated the new principle as a 2D problem. We have shown in this article that the assumption of 2D wave propagation is effective for field data. Also, the geometry of the reference receiver array and the observation point can be arbitrary. In this regard, a similar concept, but using a conventional integral representation for Green's function retrieval, was proposed earlier for reflected waves where the reference receiver array and the observation points are co-located in a horizontal borehole[49]. Also, this newly found principle can be applied to seismological monitoring using surface-waves and 2D seismometer arrays because single-mode surface waves in 3D elastic media can be represented by 2D wave propagation at the surface[50]. The independence of the estimated localized sensitivity from source locations and heterogeneities around the source points is attractive for ambient noise tomography, where the limitation due to uneven distribution of noise sources and due to heterogeneities outside the target area is especially detrimental to imaging and monitoring[51]. The novel principle can also be extended to 3D wave propagation. In that case, one needs to measure waves at a reference receiver array located over a 2D surface.

The novel principle provides a unique opportunity in case the wave source does not illuminate a medium from a location which is close to the target area, but multiple observation points are used to enhance the localization of the sensitivity without the need to know precisely the structures outside the target area. We have illustrated that this principle is

especially useful in monitoring, where the subsurface is illuminated by distant sources and the response is observed by embedded sensors. In other disciplines, this may necessitate a new data-acquisition design. In this regard, the development of fiber optic sensing has lately demonstrated that existing telecommunication networks can turn into spatially dense, subsurface acoustic sensors without a need of additional sensor installation[13,52]. The novel principle can, therefore, be powerful in future seismic monitoring in areas with difficult access, e.g., in urban or underwater environments. We anticipate that the novel principle will open up possibilities for new experiments and measurement techniques where accurate and efficient monitoring is of high importance but the conventional approaches using scattered waves are hindered by the insensitivity to the target area due to limitations in data-acquisition geometry or a poor knowledge about changes occurring outside the target zone.

Methods

Boundary integral representation

The following boundary integral representation is used to calculate the waveform at the observation point at P due to the source point at S using interferences of the observed waveforms at the reference receiver array:

$$p(P,S) = \frac{-1}{j\omega\rho} \oint_{\partial D} \sum_{i=1}^{2} n_i \partial_i G(x,P) p(x,S)\, ds, \quad (1)$$

where all properties are in the space-frequency domain, ω is the angular frequency, j the imaginary unit, ρ the density, ds the line element, and n_i the outward pointing normal vector on the arbitrary integral path ∂D, which is the location of a reference receiver array. Equation (1) indicates that the multiplication of the observed waveform, $p(x, S)$ where $x \in \partial D$, at the receiver in the reference array and the spatial derivative of the Green's function, $\partial_i G(x, P)$, in the i direction due to a point source at P, and collecting its contributions from all receivers

calculate the observed waveform at P. We derive equation (1) from the general wavefield representation[53] by defining the Green's function such that the velocity structure is same as that of the observed data, but with the Dirichlet (sound-soft) boundary condition at ∂D. This additional boundary condition correctly handles outward propagating waves at the reference receiver array by canceling non-physical wave arrivals while evaluating the integral. Furthermore, it enables us to require only single component wavefield to measure (e.g., pressure field instead of pressure and particle velocity fields), or an approximation due to the single component measurements is not necessary. This contrasts from other similar techniques of wavefield retrieval[46,47]. Furthermore, the boundary condition enables us to use model information only inside the reference receiver array because waves in impulse responses (Green's function) do not radiate outward from the boundary.

The array shape in equation (1) is arbitrary. We consider a special case of a vertical line (Fig. 1a). Suppose that a source S is located to the right of the reference receiver array, and the observation point P is located to the left of the reference receiver array. In this configuration, equation (1) can be written as

$$p(P,S) = \frac{1}{j} \int_1 G(x,P) p_{obs}(x,S)\, ds\,, \tag{2}$$

where p_{obs} is the observed waveform at the reference receiver array, G is the Green's function with the Dirichlet boundary condition at the horizontal location of the reference receiver array (Fig. 1a), and we used the relation $(n_1, n_2) = (1, 0)$.

The localized sensitivity using the adjoint of the boundary integral representation

A sensitivity of the scattered wave is defined as the change of a selected feature due to model perturbation. In this study, we consider the difference between calculated and observed waveform as,

$$E(m) = \frac{1}{2} \sum_{S,P,} \left\| p \quad p_{obs} \right\|^2 , \tag{3}$$

where $\| \|^2$ denotes the squared L2 norm and the summation takes over the number of frequencies, observation points, and source points, p and p_{obs} are respectively, calculated waveform using the boundary integral representation and observed waveform. The sensitivity is then defined as the multi-dimensional gradient of the misfit function (equation 3) with respect to the model (m), i.e., $E/\ m$. To this end, we adapt the adjoint-state method[4,30] to our problem, i.e., minimizing the misfit function (equation 3) with the wave equation and the boundary integral representation (equation 1) as constraints. We first spatially discretize the boundary integral representation (equation 1) as,

$$p_{SP} = \mathbf{p}_S \mathbf{g}_P \ , \tag{4}$$

where variables with subscript S indicate that they depend on the source location, those with subscript P indicate that they depend on the receiver location or the observation point P, and the frequency dependence of all variables is omitted for brevity. In equation (4), a column vector $\mathbf{g}_P$ is a solution to the wave equation[31]:

$$\mathbf{A}(m)\mathbf{g}_P = \mathbf{f}_P \ , \tag{5}$$

where $\mathbf{A}$ represents the discretized Helmholtz operator which is a square matrix including the spatial distribution of material properties (acoustic velocity and density), finite-difference operator, and the free-surface boundary conditions at ∂D. A column vector $\mathbf{f}_P$ includes the discretized Dirac delta function at P. A row vector $\mathbf{p}_S$ in equation (4) approximates the spatial integral in equation (1): it includes the finite-difference approximation of spatial differentiation, the multiplication of data at the receiver array $p(x, S)$, and scaling of $-1/(j\omega\rho)$ assuming homogeneous density at ∂D.

The adjoint-state method provides an algorithm which calculates efficiently the gradient[4,30]. To this end, we define the Lagrangian of our problem (equations 3, 4, and 5) as,

$$L(\tilde{p}_{SP},\tilde{\mathbf{g}}_P,\tilde{\lambda}_1,\tilde{\lambda}_2,m)=\frac{1}{2}\sum_{S,P,\omega}\left\|\tilde{p}_{SP}-p_{SP}^{obs}\right\|^2-\sum_{S,P,\omega}\tilde{\lambda}_1\left(\tilde{p}_{SP}-\mathbf{p}_S\tilde{\mathbf{g}}_P\right)-\sum_{S,P,\omega}\tilde{\lambda}_2^T\left(\mathbf{A}(m)\tilde{\mathbf{g}}_P-\mathbf{f}_P\right), \quad (6)$$

where the tilde "~" is introduced in order to distinguish between the physical realization and any element in the state and adjoint-state variable spaces, and $\tilde{\lambda}_1$ and $\tilde{\lambda}_2$ are the Lagrange multipliers. A saddle point of the Lagrangian provides the gradient of the misfit function represented by the adjoint-state variables[30]. The saddle point of the Lagrangian can be written as,

$$\frac{}{m}L(p_{SP},\mathbf{g}_P,\ _1,\ _2,m)=\frac{E}{m}=\ _{S,P,}\ ^T_2\frac{\mathbf{A}}{m}\mathbf{g}_P\ . \quad (7)$$

The real part is taken in the right-hand side term of above equation because $E(m)$ is real[30]. In the above equation, the adjoint-state variables (λ_1, λ_2) satisfy the following adjoint-state equations:

$$^T_2\mathbf{A}(m)=\ _1\mathbf{p}_S, \quad (8)$$

$$_1=\begin{pmatrix}p_{SP} & p_{SP}^{obs}\end{pmatrix}, \quad (9)$$

where * denotes the complex conjugation. These equations provide an algorithm to calculate the localized sensitivity. In order to interpret physically the adjoint-state equations, we rearrange them such that the sensitivity is a crosscorrelation of two wavefields **b** and **f**,

$$\frac{\partial E}{\partial m}=\ \sum_{S,P,}\Re\left[\mathbf{b}\ \mathbf{f}\right], \quad (10)$$

where **f** is a column vector representing the scaled forward propagating wavefield $\mathbf{g}_P$ (equation 5) from the observation point P,

$$\mathbf{f}=\frac{\mathbf{A}}{m}\mathbf{g}_P, \quad (11)$$

where the term $\mathbf{A}/\ m$ compensates for the scattering radiation pattern due to different parameterization, and **b** is a row vector representing the backward propagating wavefield defined as,

$$\mathbf{A}\ \mathbf{b} = \left(p_{SP} \quad p_{SP}^{obs} \right) \mathbf{p}_S . \tag{12}$$

The backward propagating wavefield **b** is a solution to the conjugate (time-reversed) wave equation where the source term represents the scattered waves (i.e., difference between calculated and observed waveforms) crosscorrelated with the observed waves at the reference receiver array. Note that the modeling operator **A** in equation (12) is the same as in equation (5) where the Dirichlet boundary condition at ∂D is considered.

Field experiment

The test site is made of sedimentary layers. Two instrumented vertical boreholes with 50 m horizontal separation are available. Hydrophone strings, installed in 28 m – 170 m depth range with 2 m separation between two adjacent hydrophones, are used to measure the pressure wavefield due to a surface source, simultaneously in the two boreholes. We use a small amount (6 g) of explosives for surface sources. The measurement-depth interval is split into four sections. The receiver arrays (hydrophone strings) are installed simultaneously at one of the sections in each borehole; they measure the pressure wavefield due to the surface source. In order to cover the measurement-depth interval, we repeat this procedure four times at the fixed source location changing the depth of the receiver arrays. The total recording length is 0.4 s with a sampling interval of 0.25 ms.

Waveform inversion

We use the quasi-Newton *l*-BFGS method[54,55] in estimating the velocity model by waveform inversion. The model parameter is iteratively updated using the following formula:

$$m_{k+1} = m_k \qquad {}_k Q_k \frac{E(m_k)}{m}, \tag{13}$$

where Q_k is the approximate Hessian inverse computed using previous values of the gradient, and α_k is the step length in the line-search in the descent direction.

Data Availability

The datasets generated during and/or analysed during the current study are available from the corresponding author on reasonable request.

References

1. Colton, D. & Kress, R. *Inverse acoustic and electromagnetic scattering theory*. vol. 93 (Springer Nature, 2019).

2. Wu, R. S. & Aki, K. Scattering characteristics of elastic waves by an elastic heterogeneity. *Geophysics* **50**, 582–595 (1985).

3. Habashy, T. M., Groom, R. W. & Spies, B. R. Beyond the Born and Rytov approximations: A nonlinear approach to electromagnetic scattering. *J. Geophys. Res. (Solid Earth)* **98**, 1759–1775 (1993).

4. Tromp, J. Seismic wavefield imaging of Earth's interior across scales. *Nat. Rev. Earth Environ.* **1**, 40–53 (2020).

5. Tarantola, A. Inversion of seismic reflection data in the acoustic approximation. *Geophysics* **49**, 1259–1266 (1984).

6. Virieux, J. & Operto, S. An overview of full-waveform inversion in exploration geophysics. *Geophysics* **74**, WCC1–WCC26 (2009).

7. Nikolova, N. K. Microwave imaging for breast cancer. *IEEE Microw. Mag.* **12**, 78–94 (2011).

8. Wiskin, J., Borup, D. T., Johnson, S. A. & Berggren, M. Non-linear inverse scattering: high resolution quantitative breast tissue tomography. *J. Acoust. Soc. Am.* **131**, 3802–3813 (2012).

9. Fichtner, A., Kennett, B. L. N., Igel, H. & Bunge, H. P. Theoretical background for continental-and global-scale full-waveform inversion in the time–frequency domain. *Geophys. J. Int.* **175**, 665–685 (2008).

10. Klotzsche, A., Jan van der Kruk, Niklas Linde, Joseph Doetsch & Harry Vereecken. 3-D characterization of high-permeability zones in a gravel aquifer using 2-D crosshole GPR full-waveform inversion and waveguide detection. *Geophys. J. Int.* **195**, 932–944 (2013).

11. Wai-Lok Lai, W., Dérobert, X. & Annan, P. A review of Ground Penetrating Radar application in civil engineering: A 30-year journey from Locating and Testing to Imaging and Diagnosis. *NDT E Int.* **96**, 58–78 (2018).

12. Shapiro, N. M., Campillo, M., Stehly, L. & Ritzwoller, M. H. High-resolution surface-wave tomography from ambient seismic noise. *Science.* **307**, 1615–1618 (2005).

13. Lindsey, N. J., Craig Dawe, T. & Ajo-Franklin, J. B. Illuminating seafloor faults and ocean dynamics with dark fiber distributed acoustic sensing. *Science.* **366**, 1103–1107 (2019).

14. Daley, T. M. *et al.* Field testing of fiber-optic distributed acoustic sensing (DAS) for subsurface seismic monitoring. *Lead. Edge* **32**, 699–706 (2013).

15. Binley, A., Winship, P., Middleton, R., Pokar, M. & West, J. High-resolution

characterization of vadose zone dynamics using cross-borehole radar. *Water Resour. Res.* **37**, 2639–2652 (2001).

16. Drinkwater, B. W. & Wilcox, P. D. Ultrasonic arrays for non-destructive evaluation: A review. *NDT E Int.* **39**, 525–541 (2006).

17. Poeggel, S. *et al.* Optical fibre pressure sensors in medical applications. *Sensors (Switzerland)* **15**, 17115–17148 (2015).

18. Lynch, J. P., Wang, Y., Loh, K. J., Yi, J. H. & Yun, C. B. Performance monitoring of the Geumdang Bridge using a dense network of high-resolution wireless sensors. *Smart Mater. Struct.* **15**, 1561–1575 (2006).

19. Gruber, F. K., Marengo, E. A. & Devaney, A. J. Time-reversal imaging with multiple signal classification considering multiple scattering between the targets. *J. Acoust. Soc. Am.* **115**, 3042–3047 (2004).

20. Gemmeke, H. & Ruiter, N. V. 3D ultrasound computer tomography for medical imaging. *Nucl. Instrum. Methods Phys. Res. A.* **580**, 1057–1065 (2007).

21. Rabut, C. *et al.* 4D functional ultrasound imaging of whole-brain activity in rodents. *Nat. Methods* **16**, 994–997 (2019).

22. Daley, T. M., Myer, L. R., Peterson, J. E., Majer, E. L. & Hoversten, G. M. Time-lapse crosswell seismic and VSP monitoring of injected CO2 in a brine aquifer. *Environ. Geol.* **54**, 1657–1665 (2008).

23. Ikuta, R., Yamaoka, K., Miyakawa, K., Kunitomo, T. & Kumazawa, M. Continuous monitoring of propagation velocity of seismic wave using ACROSS. *Geophys. Res. Lett.* **29**, (2002).

24. Mateeva, A. *et al.* Distributed acoustic sensing for reservoir monitoring with vertical seismic profiling. *Geophys. Prospect.* **62**, 679–692 (2014).

25. Morse, P. M. & Feshbach, H. Methods of theoretical physics. *Am. J. Phys.* **22**, 410–413 (1954).

26. Slob, E., Sato, M. & Olhoeft, G. Surface and borehole ground-penetrating-radar developments. *Geophysics* **75**, 75A103–75A120 (2010).

27. Meaney, P. M., Paulsen, K. D., Chang, J. T., Fanning, M. W. & Hartov, A. Nonactive antenna compensation for fixed-array microwave imaging: Part II–Imaging results. *IEEE Trans. Med. Imaging* **18**, 508–518 (1999).

28. Garcia-Pardo, C. *et al.* Ultrawideband technology for medical in-body sensor networks: An overview of the human body as a propagation medium, phantoms, and approaches for propagation analysis. *IEEE Antennas Propag. Mag.* **60**, 19–33 (2018).

29. Snieder, R. Extracting the Green's function from the correlation of coda waves: A derivation based on stationary phase. *Phys. Rev. E* **69**, 46610 (2004).

30. Plessix, R. E. A review of the adjoint-state method for computing the gradient of a

functional with geophysical applications. *Geophys. J. Int.* **167**, 495–503 (2006).

31. Pratt, G., Shin, C. & Hicks. Gauss-Newton and full Newton methods in frequency-space seismic waveform inversion. *Geophys. J. Int.* **133**, 341–362 (1998).

32. Sirgue, L. & Pratt, R. G. Efficient waveform inversion and imaging: A strategy for selecting temporal frequencies. *Geophysics* **69**, 231–248 (2004).

33. Landrø, M. Repeatability issues of 3-D VSP data. *Geophysics* **64**, 1673–1679 (1999).

34. Sheng, Z. An aquifer storage and recovery system with reclaimed wastewater to preserve native groundwater resources in El Paso, Texas. *J. Environ. Manage.* **75**, 367–377 (2005).

35. Almalki, M., Harris, B. & Dupuis, J. C. Field and synthetic experiments for virtual source crosswell tomography in vertical wells: Perth Basin, Western Australia. *J. Appl. Geophys.* **98**, 144–159 (2013).

36. Evans, K. F., Zappone, A., Kraft, T., Deichmann, N. & Moia, F. A survey of the induced seismic responses to fluid injection in geothermal and CO2 reservoirs in Europe. *Geothermics* **41**, 30–54 (2012).

37. Lumley, D. E. Time-lapse seismic reservoir monitoring. *Geophysics* **66**, 50–53 (2001).

38. Arts, R. *et al.* Monitoring of CO2 Injected at Sleipner Using Time Lapse Seismic Data. *Greenh. Gas Control Technol. - 6th Int. Conf.* 347–352 (2003) doi:10.1016/b978-008044276-1/50056-8.

39. Christensen, N. I. & Wang, H. F. The Influence of pore pressure and confining pressure on dynamic elastic properties of Berea sandstone. *Geophysics* **50**, 207–213 (1985).

40. Lu, Z. & Sabatier, J. M. Effects of soil water potential and moisture content on sound speed. *Soil Sci. Soc. Am. J.* **73**, 1614–1625 (2009).

41. Lobkis, O. I. & Weaver, R. L. On the emergence of the Green's function in the correlations of a diffuse field. *J. Acoust. Soc. Am.* **110**, 3011–3017 (2001).

42. Snieder, R., Miyazawa, M., Slob, E., Vasconcelos, I. & Wapenaar, K. A comparison of strategies for seismic interferometry. *Surv. Geophys.* **30**, 503–523 (2009).

43. Michaels, J. E. & Michaels, T. E. Detection of structural damage from the local temporal coherence of diffuse ultrasonic signals. *IEEE Trans. Ultrason. Ferroelectr. Freq. Control* **52**, 1769–1782 (2005).

44. Sabra, K. G., Conti, S., Roux, P. & Kuperman, W. A. Passive in vivo elastography from skeletal muscle noise. *Appl. Phys. Lett.* **90**, 1–4 (2007).

45. Wapenaar, K. *et al*. Seismic interferometry by crosscorrelation and by multidimensional deconvolution: a systematic comparison. *Geophys. J. Int.* **185**, 1335–1364 (2011).

46. van der Neut, J., Thorbecke, J., Mehta, K., Slob, E. & Wapenaar, K. Controlled-source interferometric redatuming by crosscorrelation and multidimensional deconvolution in elastic media. *Geophysics* **76**, SA63–SA76 (2011).

47. Minato, S. *et al*. Seismic interferometry using multidimensional deconvolution and crosscorrelation for crosswell seismic reflection data without borehole sources. *Geophysics* **76**, SA19–SA34 (2011).

48. Ramirez, A. C. & Weglein, A. B. Green's theorem as a comprehensive framework for data reconstruction, regularization, wavefield separation, seismic interferometry, and wavelet estimation: A tutorial. *Geophysics* **74**, W35–W62 (2009).

49. da Costa, C. A. N., Costa, J. C., Medeiros, W. E., Verschuur, D. J. & Soni, A. K. Target-level waveform inversion: a prospective application of the convolution-type representation for the acoustic wavefield. *Geophys. Prospect.* **67**, 69–84 (2018).

50. Tanimoto, T. Modelling curved surface wave paths: membrane surface wave synthetics. *Geophys. J. Int.* **102**, 89–100 (1990).

51. Sager, K., Ermert, L., Boehm, C. & Fichtner, A. Towards full waveform ambient noise inversion. *Geophys. J. Int.* **212**, 566–590 (2018).

52. Ajo-Franklin, J. B. *et al.* Distributed acoustic sensing using dark fiber for near-surface characterization and broadband seismic event detection. *Sci. Rep.* **9**, 1–14 (2019).

53. Wapenaar, K. General representations for wavefield modeling and inversion in geophysics. *Geophysics* **72**, SM5–SM17 (2007).

54. Nocedal, J. Updating quasi-Newton matrices with limited storage. *Math. Comput.* **35**, 773–782 (1980).

55. Métivier, L. & Brossier, R. The SEISCOPE optimization toolbox: A large-scale nonlinear optimization library based on reverse communication. *Geophysics* **81**, F1–F15 (2016).

Acknowledgements:

The work of S.M. has received financial support from OYO corporation, Japan.

Author Contributions:

S.M.: Conceptualization, Methodology, Formal Analysis, Writing – Original Draft, Writing – Review & Editing; R.G.: Discussions, Review & Editing.

Competing interests:

The authors declare no competing interests.

Figures

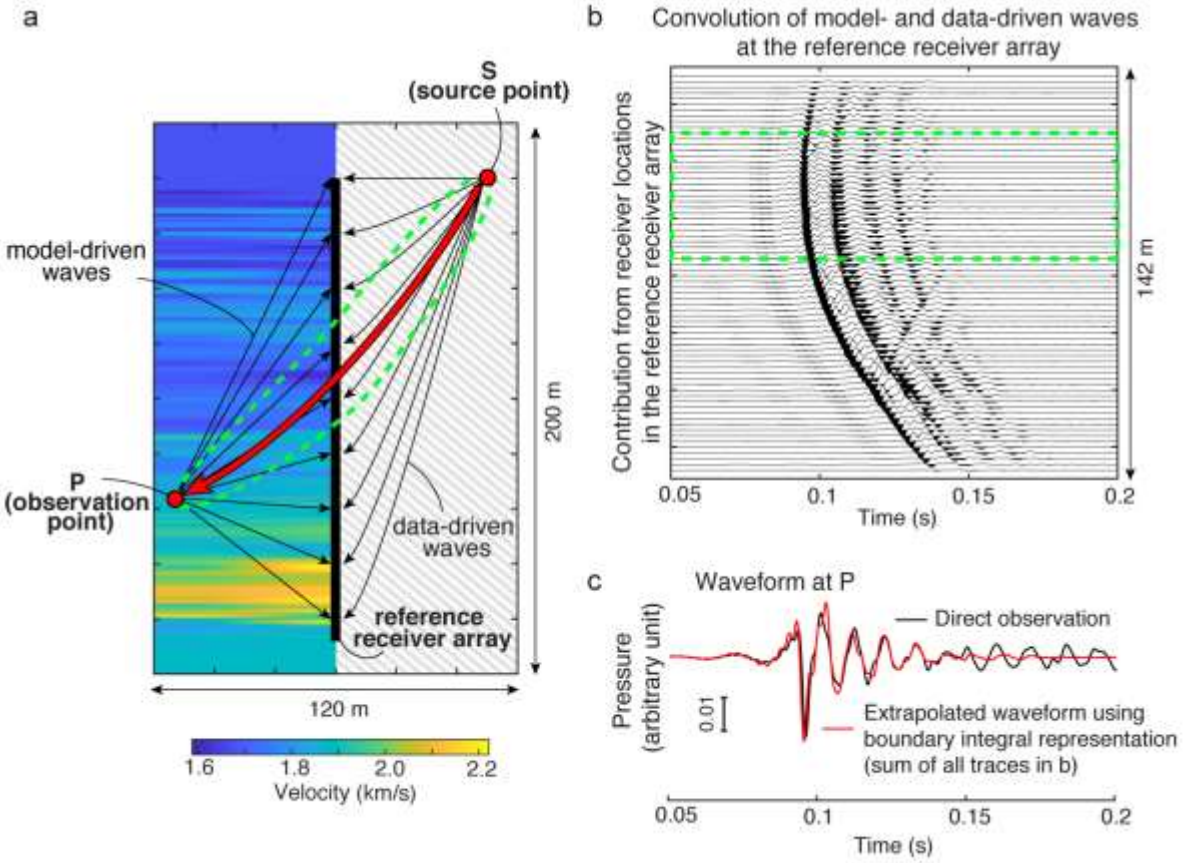

Figure. 1. Wavefield extrapolation on actual field data using the boundary integral representation. Scattered waves are observed at a reference receiver array (pressure sensors). These waves are used in the representation to calculate the response at the observation point P (wavefield extrapolation). (a) Source-observation point geometry and the velocity model assumed in calculating the "model-driven waves". The process of wavefield extrapolation and the result do not need any knowledge of the velocity model in the gray-shaded area, and all wave phenomena (transmission, scattering, dissipation) in this zone are accounted for in a data-driven manner. (b) Contribution at each receiver in the reference receiver array to the boundary integral representation, and (c) the extrapolated waveform in comparison with the directly observed one at P.

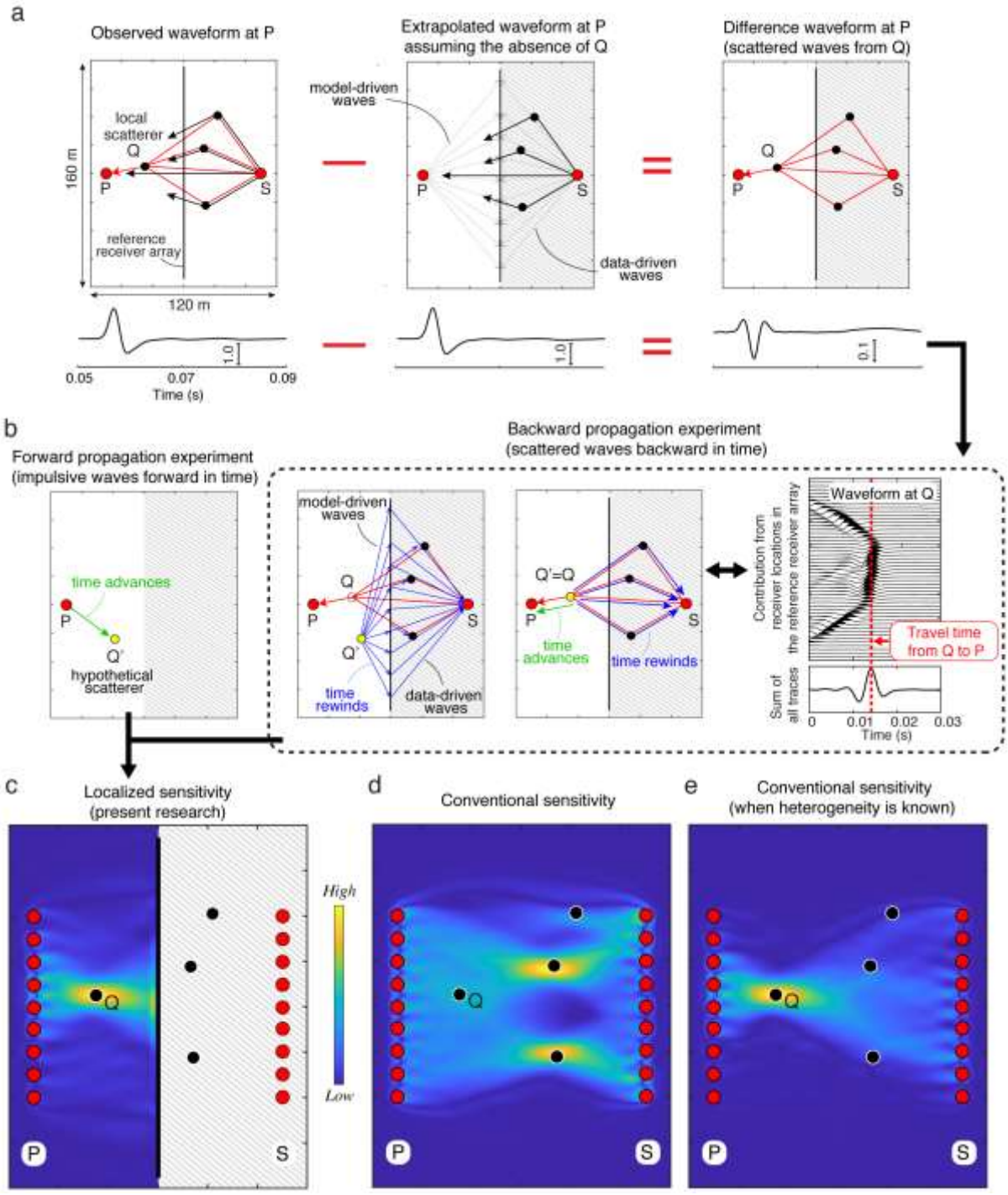

Figure. 2. A novel principle to localize the scattered-wave sensitivity: schematic illustration and results on synthetic data. (a) "Observed waveform": all waves coming from a source S are observed at an observation point (P) and a reference receiver array. Black arrows show direct and scattered waves which are not associated with the local scatter Q located close to P, and red arrows show scatterings from Q. "Extrapolated waveform": the waveform is extrapolated using the boundary integral representation assuming a material without Q.

"Difference waveform": the difference between the observed and the extrapolated waveforms containing scattered waves from Q. Gray-shaded area shows the zone which has no effect on the boundary integral representation. (b) Thought experiments of forward and backward wave propagation for calculating the localized sensitivity. The backward propagation experiment uses the difference waveform in (a) as input, and calculates the adjoint of the boundary integral representation (see main text). Both forward and backward propagation experiments are independent of the structure around the source point (gray-shaded area). (c) The localized sensitivity obtained from the correlation between the forward and backward propagating waves for various locations of the hypothetical scatterer Q'. The sensitivity using multiple source-observation points is shown. (d) The conventional sensitivity obtained using the same source-observation points as in the calculation for the localized sensitivity. (e) The conventional sensitivity when all heterogeneities/scatterers but Q are known.

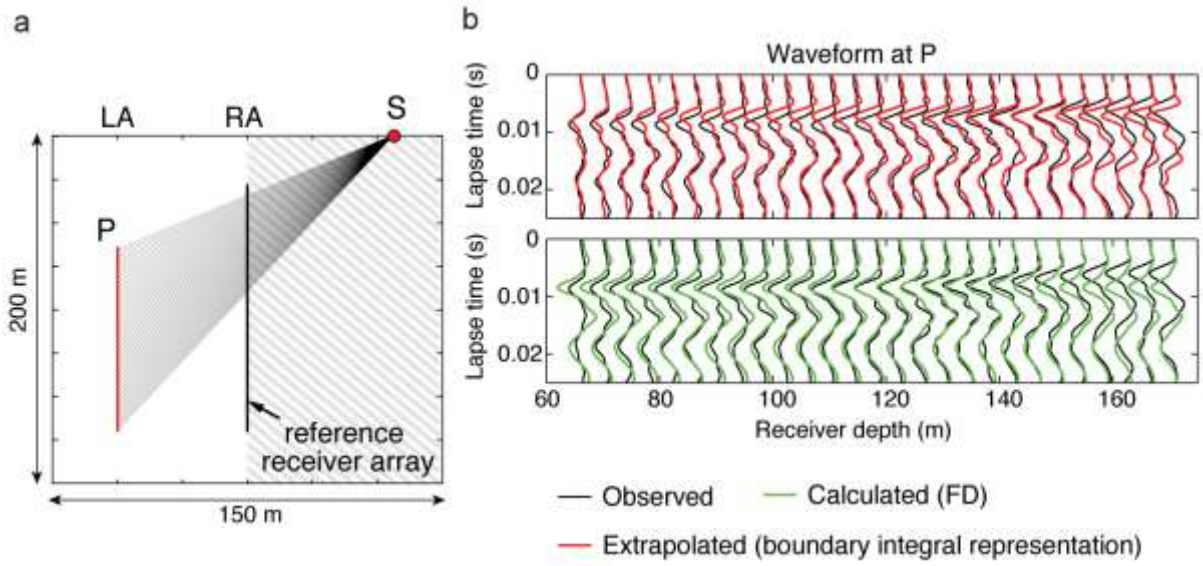

Figure. 3. Observed and calculated/extrapolated waveforms in field measurements: (a) Geometry of a surface source (S), an array of observation points (P), and a reference receiver array. Receivers are located in two vertical boreholes (LA, left array and RA, right array). (b) Observed waveform, extrapolated waveform using the boundary integral representation, and calculated waveform using conventional finite-difference method[31]. The time axis is the time lapsed since the expected arrival, assuming a constant acoustic velocity and straight propagation paths (black lines in (a)).

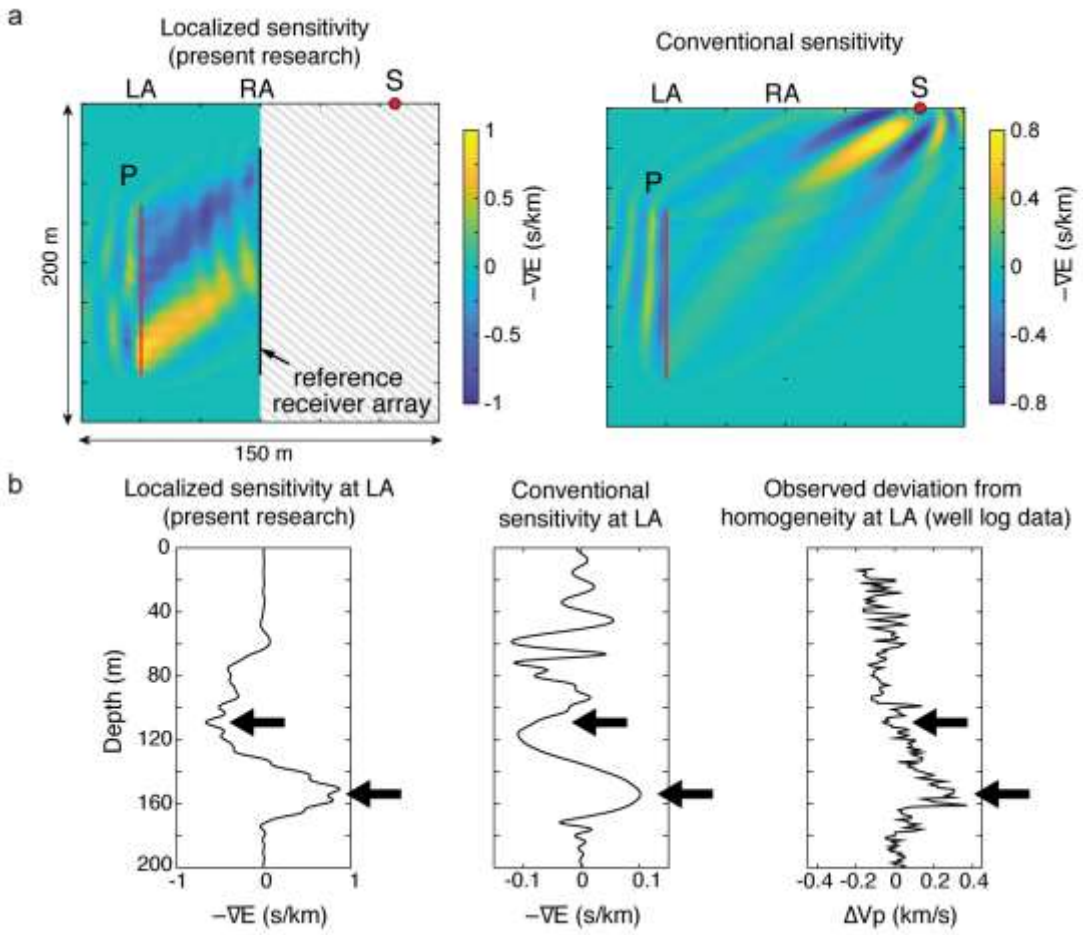

1

2 **Figure. 4.** Localized sensitivity detected in field experimental data: (a) Localized and
3 conventional sensitivity using the same source-observation points. (b) Comparison between
4 the sensitivities and the observed perturbation (well log data) in acoustic velocity from a
5 constant average value at LA. Black arrows mark the location where the localized sensitivity
6 captures a finer variation in the structure than the conventional sensitivity.

7

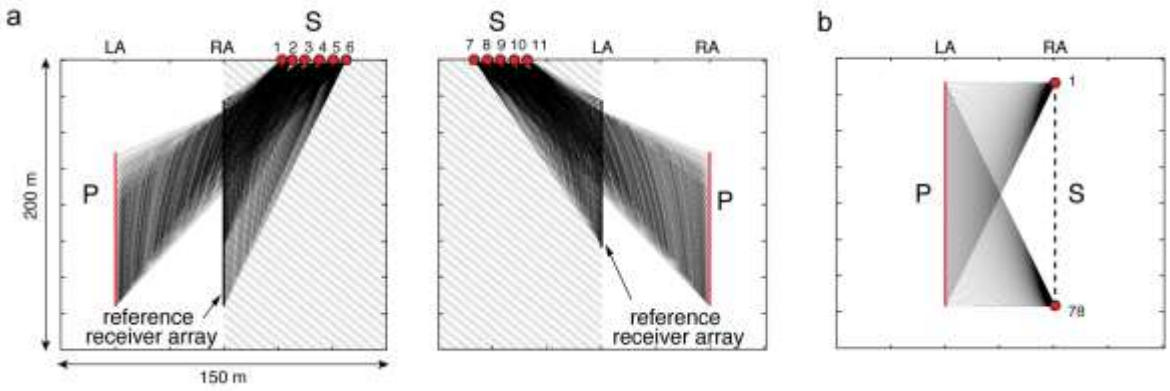

Figure. 5. Schematic illustration of field experiments with multiple source-observation points: (a) Multiple sources (S), an array of observation points (P), and the reference receiver array in the field experiments where surface sources were located on the right to RA or on the left to LA. The gray-shaded area marks the zone which has no effect on the calculated sensitivity (this research). (b) Ground-truthing measurements performed using downhole sources.

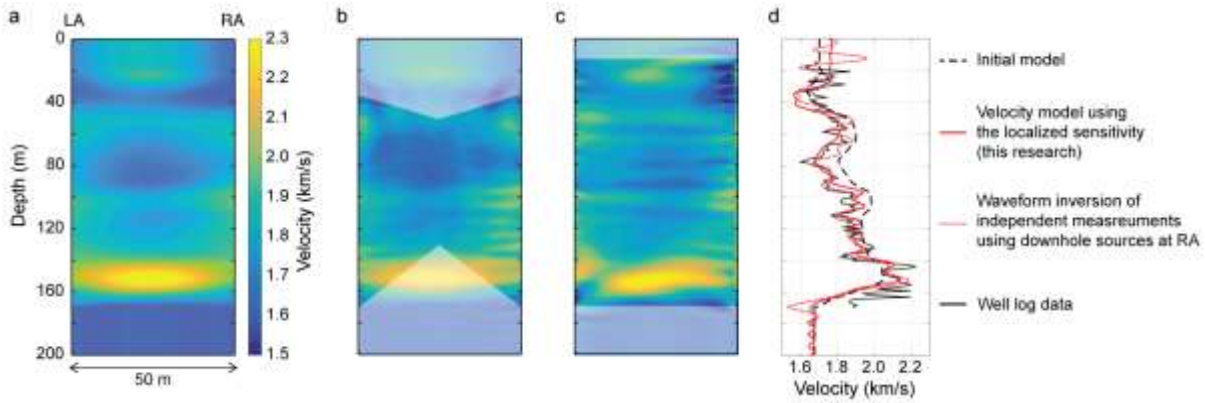

Figure. 6. Heterogeneity resolved quantitatively on field data: (a) Velocity structure derived from traveltime tomography, which is used as the initial model in waveform inversion. (b) Resolved structure using the localized sensitivity (this research). White-shaded area indicates a zone with low ray coverage. (c) Resolved structure from waveform inversion of data using downhole acoustic sources located at RA. (d) Comparison of obtained heterogeneous velocity distributions with well log data at RA.

1

2

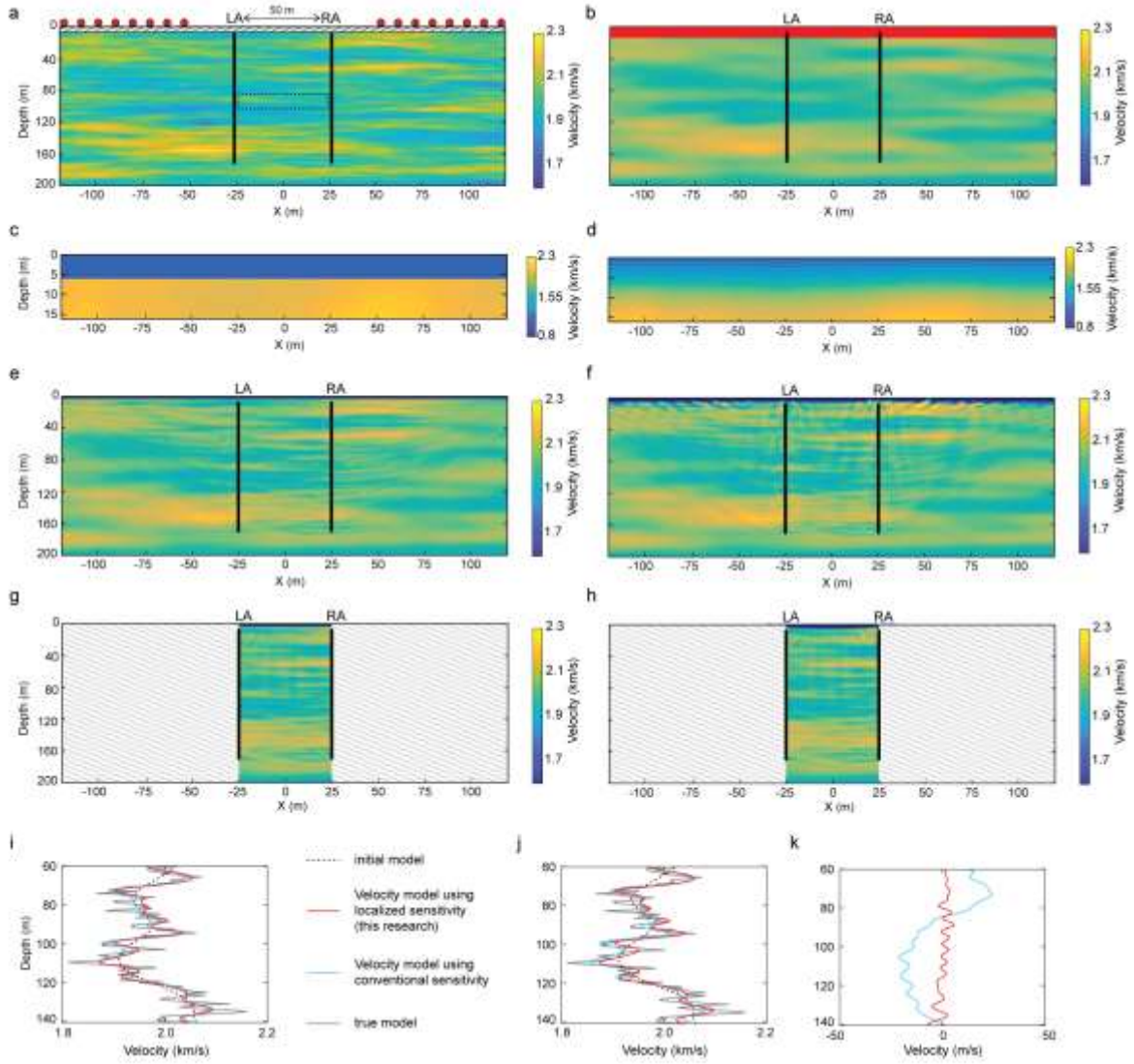

3

4 **Figure. 7.** True and resolved velocity structures in the numerical monitoring experiments
5 using waveform inversion with different accuracies in the prior knowledge of the vadose
6 zone: (a) True velocity model (baseline). The topmost layer (hatched area) is the vadose
7 zone. The dashed rectangle at 100 m depth indicates the target area where there are velocity
8 changes between the baseline and the monitor surveys due to changes in the pore pressure.
9 (b) Initial velocity model. (c) Initial velocity model for the top 16 m (red area in (b)); the
10 correct thicknesses and the correct average velocity in the vadose zone are known. (d) Same

as (c) but with poor prior information of the vadose zone. (e) Obtained result using conventional scattered-wave sensitivity when an accurate information of the vadose zone is available as in (c), and (f) the obtained result corresponding to (d). (g),(h) Same as (e) and (f) but using localized sensitivity derived from the novel principle found in this research. (i) Comparison of the resolved velocity structures at the target area at x=0 m using the prior information presented in (c), and (j) the same using prior information presented in (d). (k) Spurious velocity changes due to different accuracies in the prior knowledge of the vadose zone. The difference in the estimated velocity between (i) and (j) is shown using conventional sensitivity (blue line) and localized sensitivity (red line) of scattered waves.

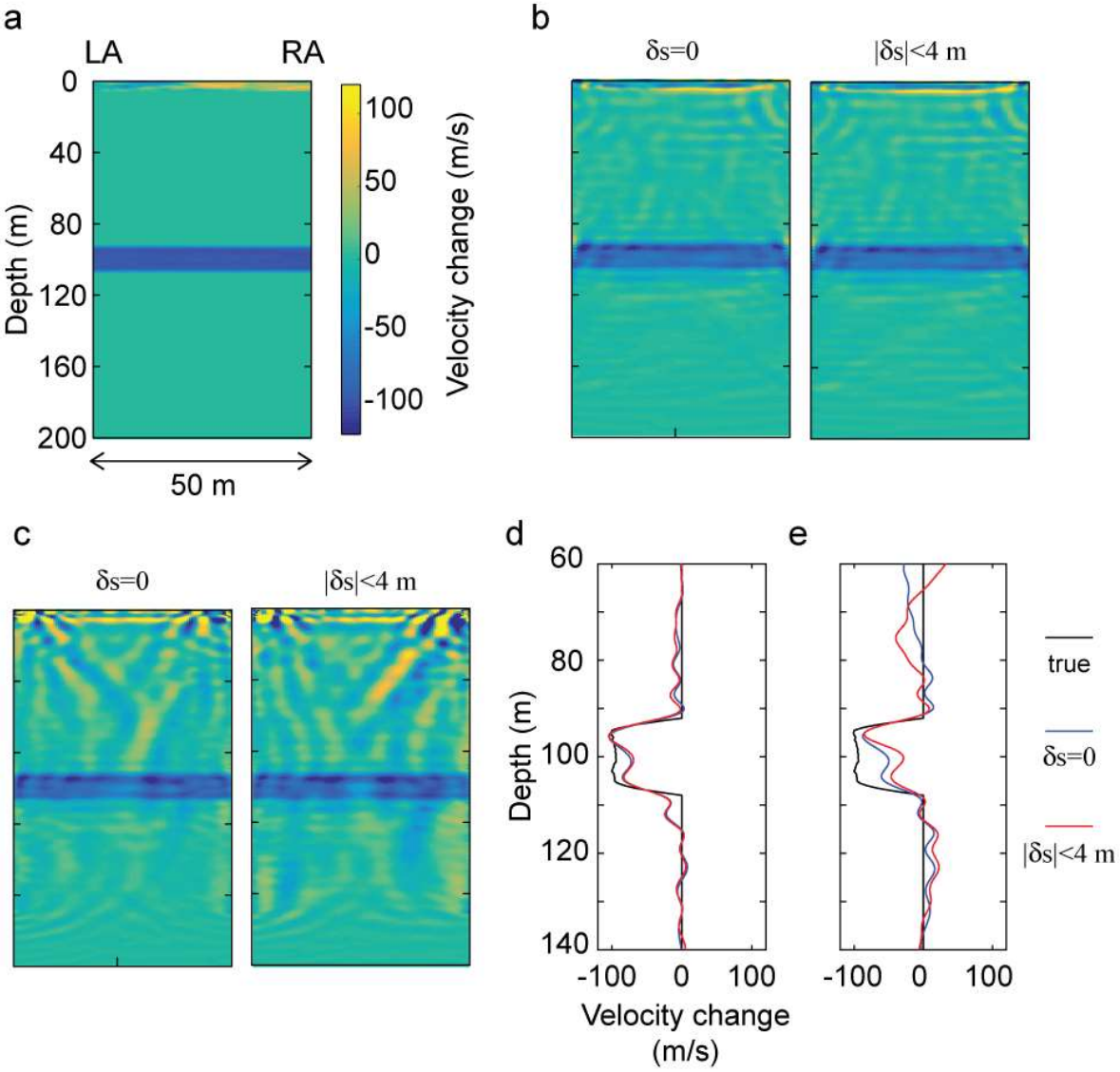

Figure. 8. Time-lapse changes at the target zone (dashed rectangle in Fig. 7(a)) : (a) True temporal changes. (b) Estimated temporal changes using the localized sensitivity for scattered waves (this research). In this case, the initial velocity model contains inaccurate prior information regarding the vadose zone (Fig. 7(d)). Results using data without source location errors (δs=0) and with source location errors (|δs| < 4 m) are shown. (c) Same as (b) but using the conventional sensitivity. (d) Estimated velocity changes in the target area at x=0 m using the localized sensitivity, and (e) the same using the conventional sensitivity.

Figures

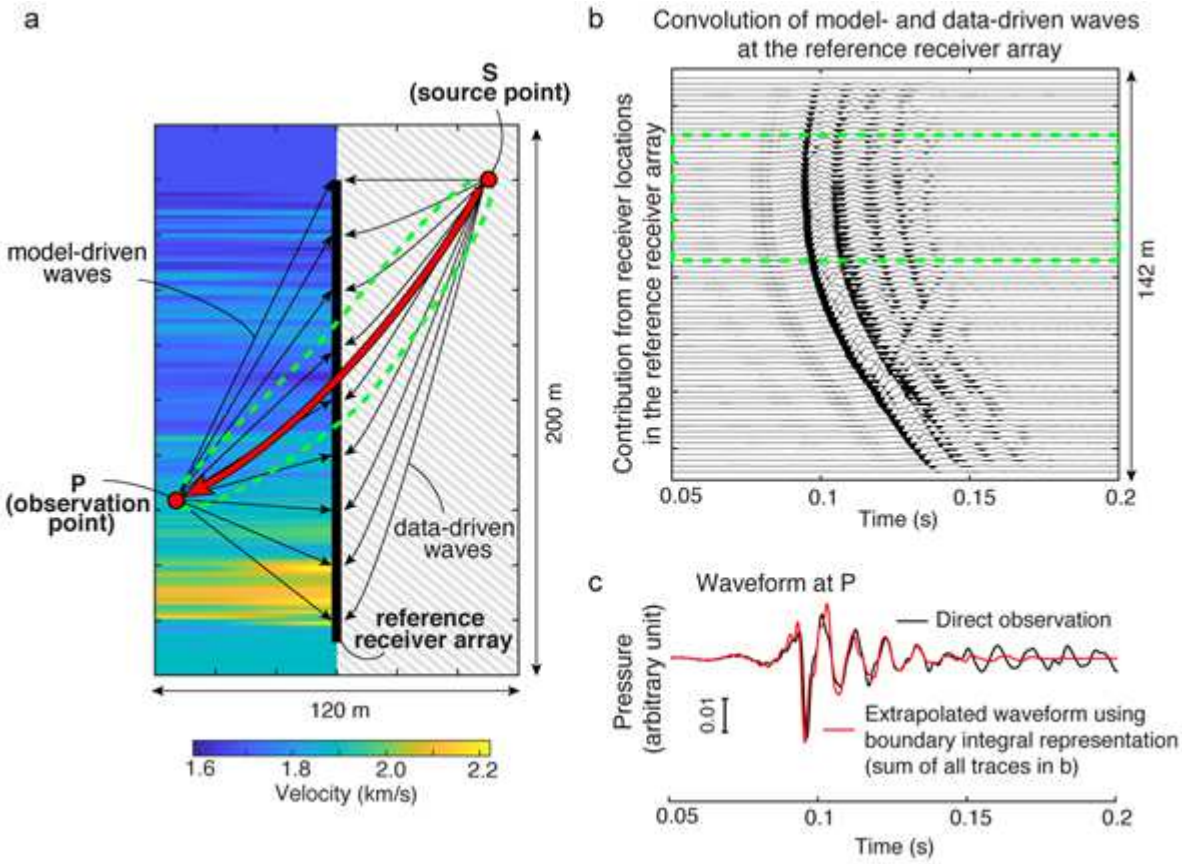

Figure 1

Wavefield extrapolation on actual field data using the boundary integral representation. Scattered waves are observed at a reference receiver array (pressure sensors). These waves are used in the representation to calculate the response at the observation point P (wavefield extrapolation). (a) Source-observation point geometry and the velocity model assumed in calculating the “model-driven waves”. The process of wavefield extrapolation and the result do not need any knowledge of the velocity model in the gray-shaded area, and all wave phenomena (transmission, scattering, dissipation) in this zone are accounted for in a data-driven manner. (b) Contribution at each receiver in the reference receiver array to the boundary integral representation, and (c) the extrapolated waveform in comparison with the directly observed one at P.

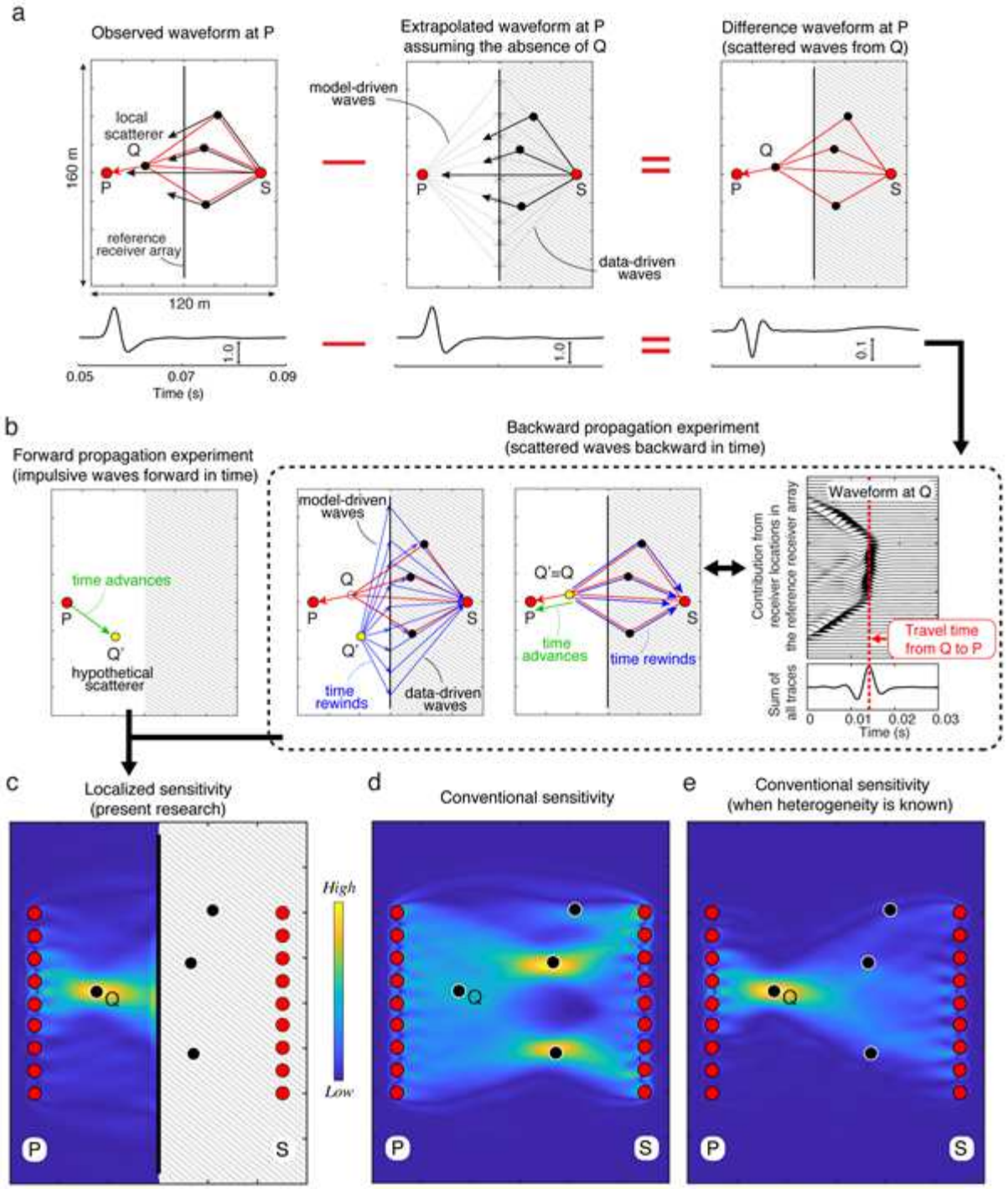

Figure 2

A novel principle to localize the scattered-wave sensitivity: schematic illustration and results on synthetic data. (a) “Observed waveform”: all waves coming from a source S are observed at an observation point (P) and a reference receiver array. Black arrows show direct and scattered waves which are not associated with the local scatter Q located close to P, and red arrows show scatterings from Q. “Extrapolated waveform”: the waveform is extrapolated using the boundary integral representation assuming a material without Q. “Difference waveform”: the difference between the observed and the extrapolated waveforms containing scattered waves from Q. Gray-shaded area shows the zone which has no effect on the boundary integral representation. (b) Thought experiments of forward and backward

wave propagation for calculating the localized sensitivity. The backward propagation experiment uses the difference waveform in (a) as input, and calculates the adjoint of the boundary integral representation (see main text). Both forward and backward propagation experiments are independent of the structure around the source point (gray-shaded area). (c) The localized sensitivity obtained from the correlation between the forward and backward propagating waves for various locations of the hypothetical scatterer Q'. The sensitivity using multiple source-observation points is shown. (d) The conventional sensitivity obtained using the same source-observation points as in the calculation for the localized sensitivity. (e) The conventional sensitivity when all heterogeneities/scatterers but Q are known.

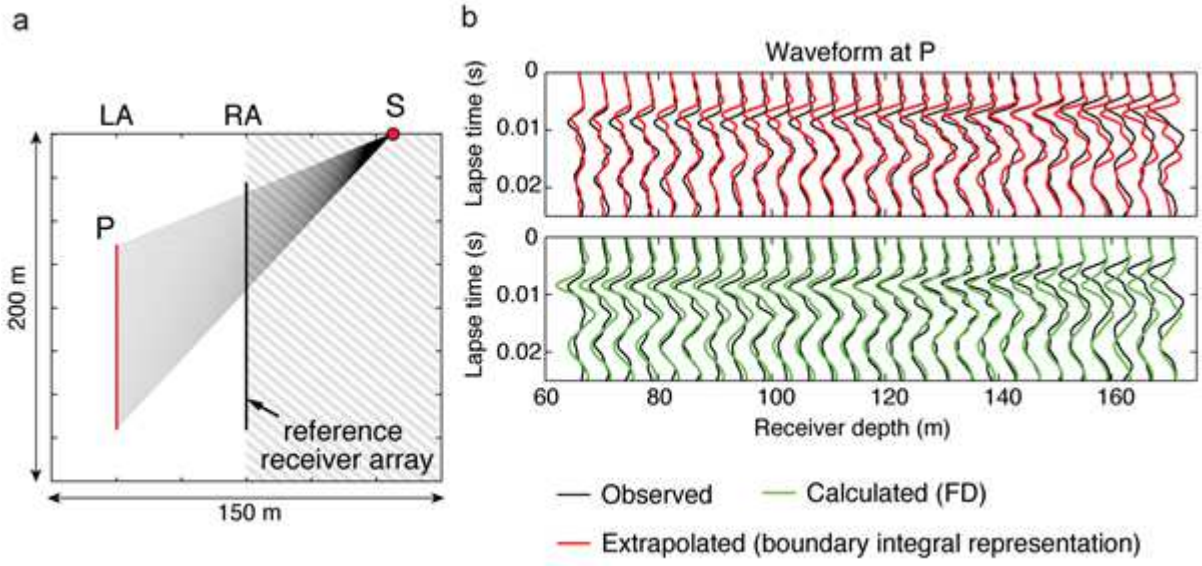

Figure 3

Observed and calculated/extrapolated waveforms in field measurements: (a) Geometry of a surface source (S), an array of observation points (P), and a reference receiver array. Receivers are located in two vertical boreholes (LA, left array and RA, right array). (b) Observed waveform, extrapolated waveform using the boundary integral representation, and calculated waveform using conventional finite-difference method31. The time axis is the time lapsed since the expected arrival, assuming a constant acoustic velocity and straight propagation paths (black lines in (a)).

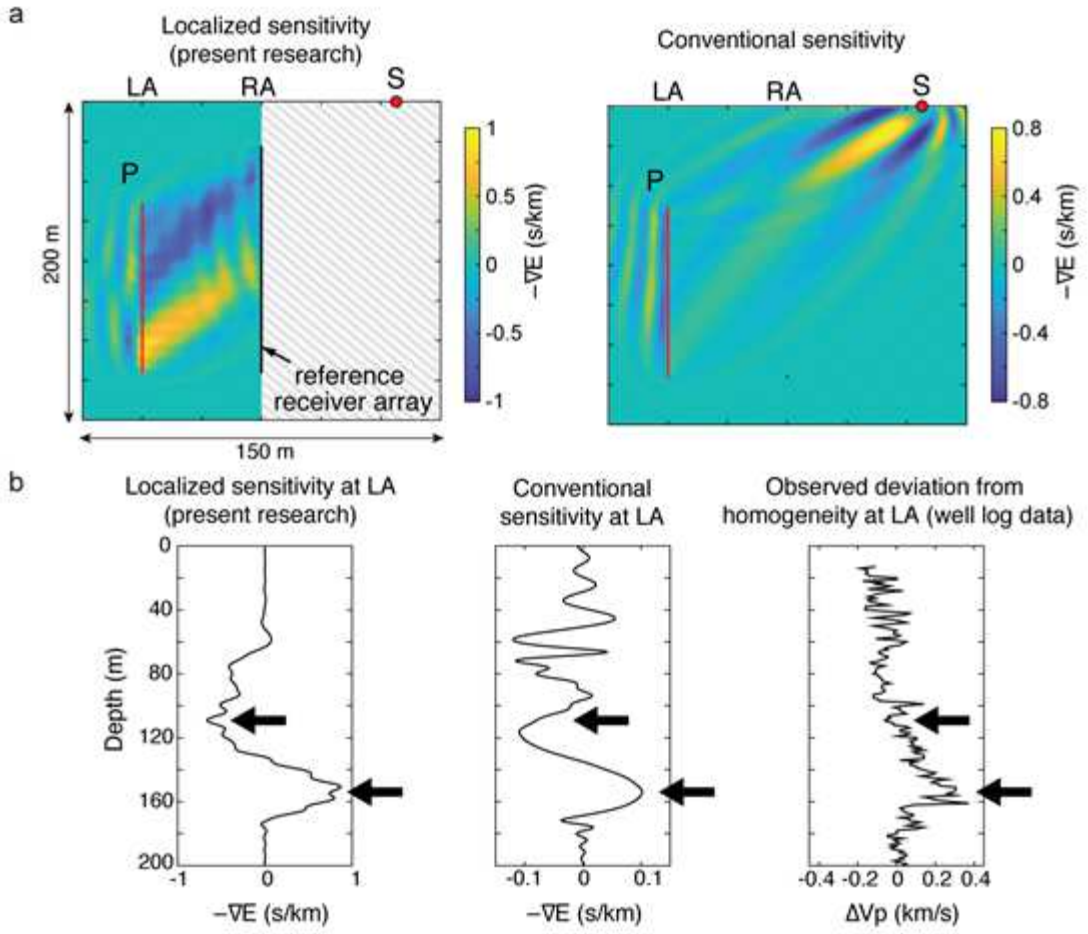

Figure 4

Localized sensitivity detected in field experimental data: (a) Localized and conventional sensitivity using the same source-observation points. (b) Comparison between the sensitivities and the observed perturbation (well log data) in acoustic velocity from a constant average value at LA. Black arrows mark the location where the localized sensitivity captures a finer variation in the structure than the conventional sensitivity.

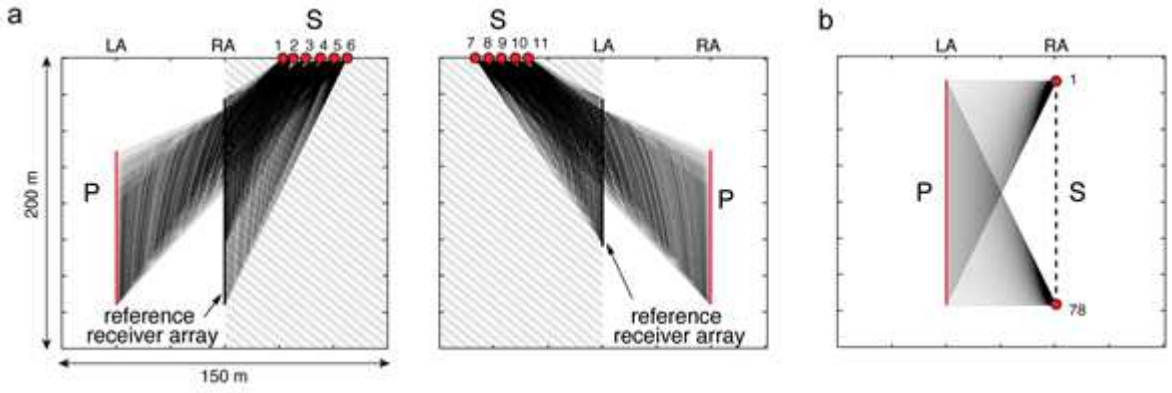

Figure 5

Schematic illustration of field experiments with multiple source-observation points: (a) Multiple sources (S), an array of observation points (P), and the reference receiver array in the field experiments where surface sources were located on the right to RA or on the left to LA. The gray-shaded area marks the zone which has no effect on the calculated sensitivity (this research). (b) Ground-truthing measurements performed using downhole sources.

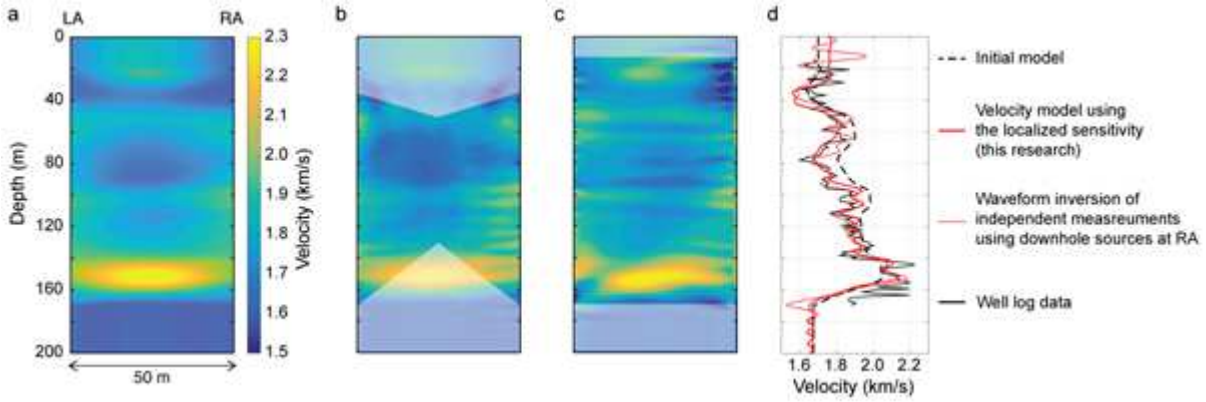

Figure 6

Heterogeneity resolved quantitatively on field data: (a) Velocity structure derived from traveltime tomography, which is used as the initial model in waveform inversion. (b) Resolved structure using the localized sensitivity (this research). White-shaded area indicates a zone with low ray coverage. (c) Resolved structure from waveform inversion of data using downhole acoustic sources located at RA. (d) Comparison of obtained heterogeneous velocity distributions with well log data at RA.

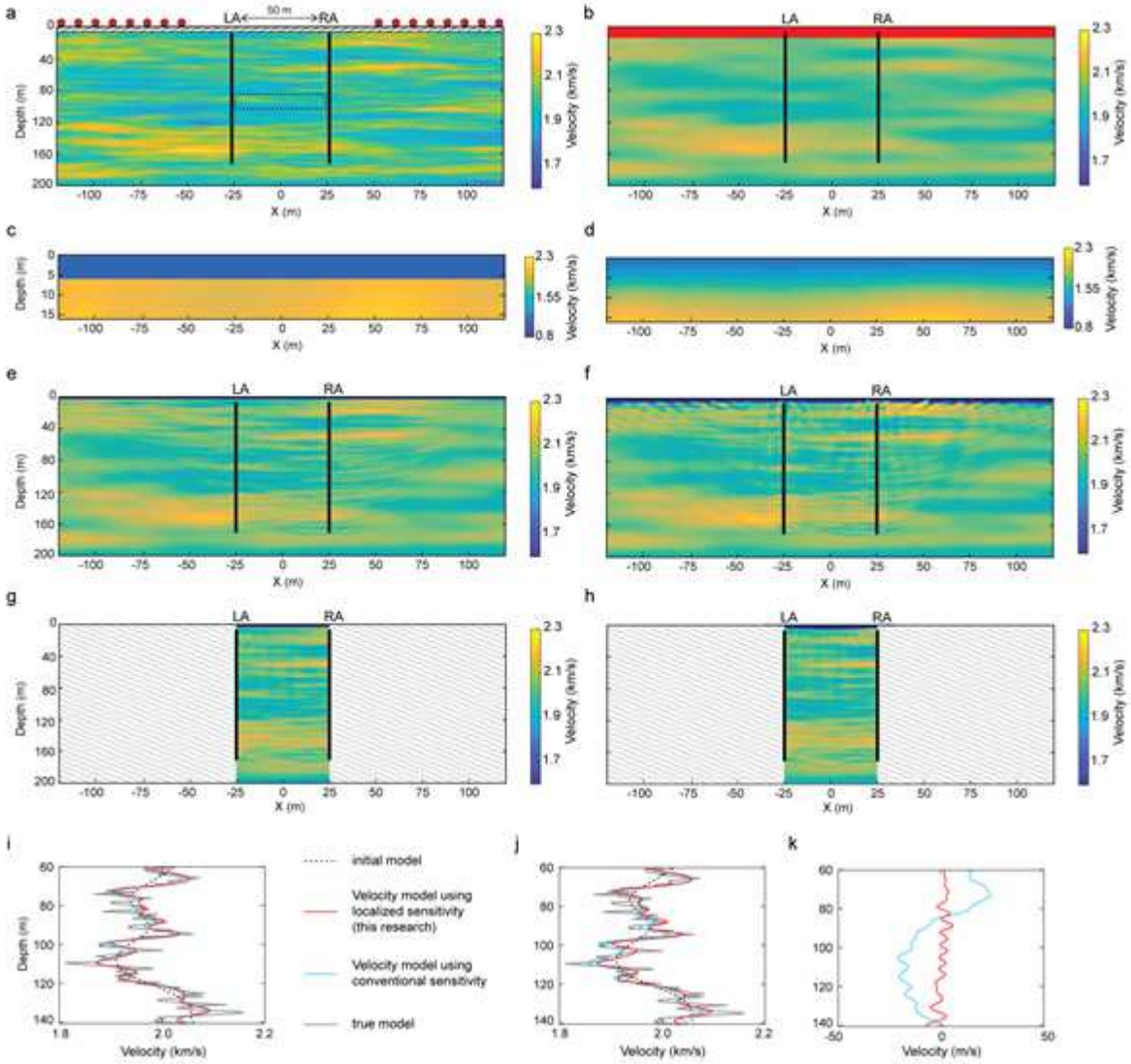

Figure 7

True and resolved velocity structures in the numerical monitoring experiments using waveform inversion with different accuracies in the prior knowledge of the vadose zone: (a) True velocity model (baseline). The topmost layer (hatched area) is the vadose zone. The dashed rectangle at 100 m depth indicates the target area where there are velocity changes between the baseline and the monitor surveys due to changes in the pore pressure. (b) Initial velocity model. (c) Initial velocity model for the top 16 m (red area in (b)); the correct thicknesses and the correct average velocity in the vadose zone are known. (d) Same as (c) but with poor prior information of the vadose zone. (e) Obtained result using conventional scattered-wave sensitivity when an accurate information of the vadose zone is available as in (c), and (f) the obtained result corresponding to (d). (g),(h) Same as (e) and (f) but using localized sensitivity derived from the novel principle found in this research. (i) Comparison of the resolved velocity structures at the target area at x=0 m using the prior information presented in (c), and (j) the same using prior information presented in (d). (k) Spurious velocity changes due to different accuracies in the prior knowledge of the vadose zone. The difference in the estimated velocity between (i) and (j) is shown using conventional sensitivity (blue line) and localized sensitivity (red line) of scattered waves.

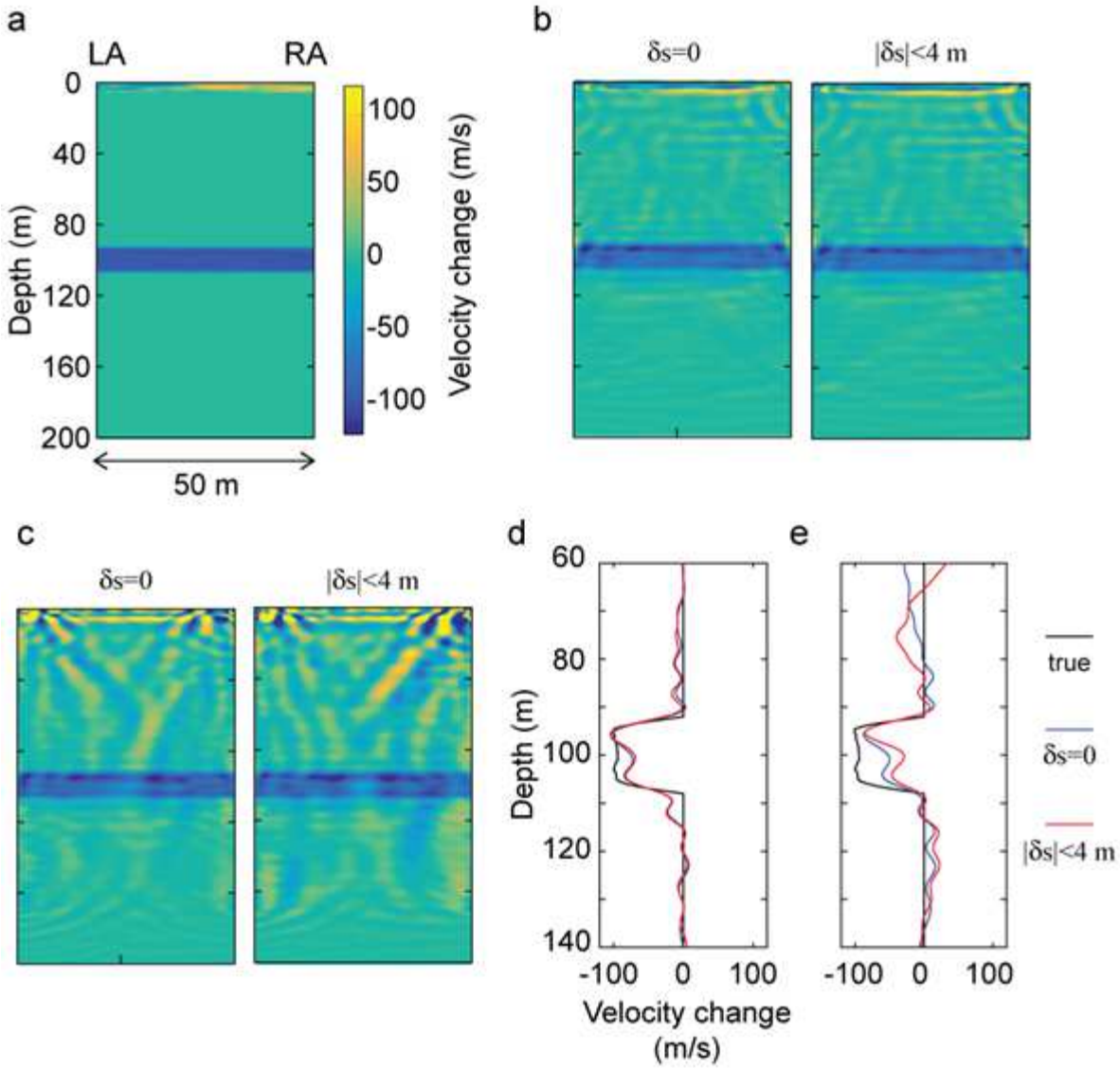

Figure 8

Time-lapse changes at the target zone (dashed rectangle in Fig. 7(a)) : (a) True temporal changes. (b) Estimated temporal changes using the localized sensitivity for scattered waves (this research). In this case, the initial velocity model contains inaccurate prior information regarding the vadose zone (Fig. 7(d)). Results using data without source location errors (□s=0) and with source location errors (|□s| < 4 m) are shown. (c) Same as (b) but using the conventional sensitivity. (d) Estimated velocity changes in the target area at x=0 m using the localized sensitivity, and (e) the same using the conventional sensitivity.

Supplementary Files

This is a list of supplementary files associated with this preprint. Click to download.

- SupplementInfo.pdf